

ARTICLE OPEN



Ultrastiff graphene

Vesa-Matti Hiltunen ¹, Pekka Koskinen ¹, Kamila K. Mentel ², Jyrki Manninen ¹, Pasi Myllyperkiö ², Mika Pettersson ² and Andreas Johansson ^{1,2}✉

Graphene has exceptionally high in-plane strength, which makes it ideal for various nanomechanical applications. At the same time, its exceptionally low out-of-plane stiffness makes it also flimsy and hard to handle, rendering out-of-plane structures unstable and difficult to fabricate. Therefore, from an application point of view, a method to stiffen graphene would be highly beneficial. Here we demonstrate that graphene can be significantly stiffened by using a laser writing technique called optical forging. We fabricate suspended graphene membranes and use optical forging to create stable corrugations. Nanoindentation experiments show that the corrugations increase graphene bending stiffness up to 0.8 MeV, five orders of magnitude larger than pristine graphene and corresponding to some 35 layers of bulk graphite. Simulations demonstrate that, in addition to stiffening by micron-scale corrugations, optical forging stiffens graphene also at the nanoscale. This magnitude of stiffening of an atomically thin membrane will open avenues for a plethora of new applications, such as GHz resonators and 3D scaffolds.

npj 2D Materials and Applications (2021)5:49; <https://doi.org/10.1038/s41699-021-00232-1>

INTRODUCTION

Modifying or enhancing mechanical properties of a material does not always require changing its internal composition. Altering the properties can be achieved also by rather simple changes of shape in the overall structure. For example, corrugated metal sheets have higher bending stiffnesses compared to their flat counterparts of the same thickness, which is why corrugated sheets are often used as roofing materials. Corrugated structures are also utilized in packaging materials, such as cardboard boxes and plastic containers.

The principle of mechanical reinforcement by corrugations can be applied equally to nanoscale materials. Graphene has a Young's modulus of 1 TPa, which makes it the strongest material in the world¹. However, as an atomically thin material, it is also very flimsy and conforms to the shapes of underlying substrates. While sometimes the low-bending stiffness of graphene is a strength, other times having a rigid structure without substrate support is advantageous. There is ample evidence that nanoscale corrugations increase the bending stiffness of graphene significantly², enabling the shaping of graphene into stable three-dimensional forms. This stiffened graphene could be used in a wide variety of nanomechanical devices, such as resonators, nanoscale springs or ultralight scaffolds.

In this study, we create corrugations to suspended graphene membranes by irradiating it with a femtosecond pulsed laser under inert atmosphere in a process that we call optical forging^{3–5}. The graphene was fabricated by chemical vapor deposition and transferred onto a silicon nitride membrane window with different-sized openings. The graphene membranes were characterized before and after optical forging with Raman spectroscopy, atomic force microscopy (AFM), and nanoindentation.

RESULTS

Effect of optical forging on suspended graphene

Figure 1 presents how optical forging modifies graphene. Before forging, the membrane is bowing downwards, as it adheres to the

sidewalls of the openings. The membrane itself is smooth, although in Fig. 1a there are a few folds and residual particles from the graphene transfer step visible. After forging, the shape of the graphene membrane has changed completely, as it bulges upwards and is extremely corrugated, while the residues are removed. There are two length scales for the corrugations. The ridges and grooves caused by the small-scale corrugations in Fig. 1b are close to vertical, corresponding to the fast scan direction of the laser writing, while the large-scale corrugation is perpendicular to it. It is notable that even though the laser writing pattern has a square shape, the graphene outside of the opening remains unchanged. This is a deviation from the behavior of graphene on plain silicon oxide, where the shape of graphene follows the laser writing pattern^{3,5}. This is presumably because of higher adhesion of graphene to silicon nitride⁶. However, the membrane in Fig. 1b has delaminated from the rim of the opening, which contributes to the final height of the corrugated graphene structure.

Raman spectra of the graphene membrane before and after optical forging are shown in Fig. 1e. The striking difference is the appearance of a sharp D-band at 1340 cm⁻¹. Before forging this band is missing, which indicates that initially the graphene is defect-free⁷. Optical forging creates lattice defects in the graphene, which we have reported previously^{3,5}. It is important to note that after optical forging the two-dimensional (2D) Raman band is still defined by a single symmetric peak and the intensity is greater than the G-band. These observations indicate that graphene is still single-layered and has long-range order, despite the increased defect concentration and the huge difference in the morphology^{7–9}.

Other differences besides the D-band intensity are shifts in the peak positions of the G and 2D Raman bands and an increase in 2D/G intensity ratio. Positions of these peaks can be used to estimate both doping and strain of graphene (see Supplementary Methods). The results show that before forging our graphene membranes are slightly compressively strained and hole-doped. Small amount of compressive strain is common for chemical vapor deposition (CVD) graphene after transfer to the final substrate¹⁰.

¹Nanoscience Center, Department of Physics, University of Jyväskylä, Jyväskylä, Finland. ²Nanoscience Center, Department of Chemistry, University of Jyväskylä, Jyväskylä, Finland. ✉email: andreas.johansson@jyu.fi

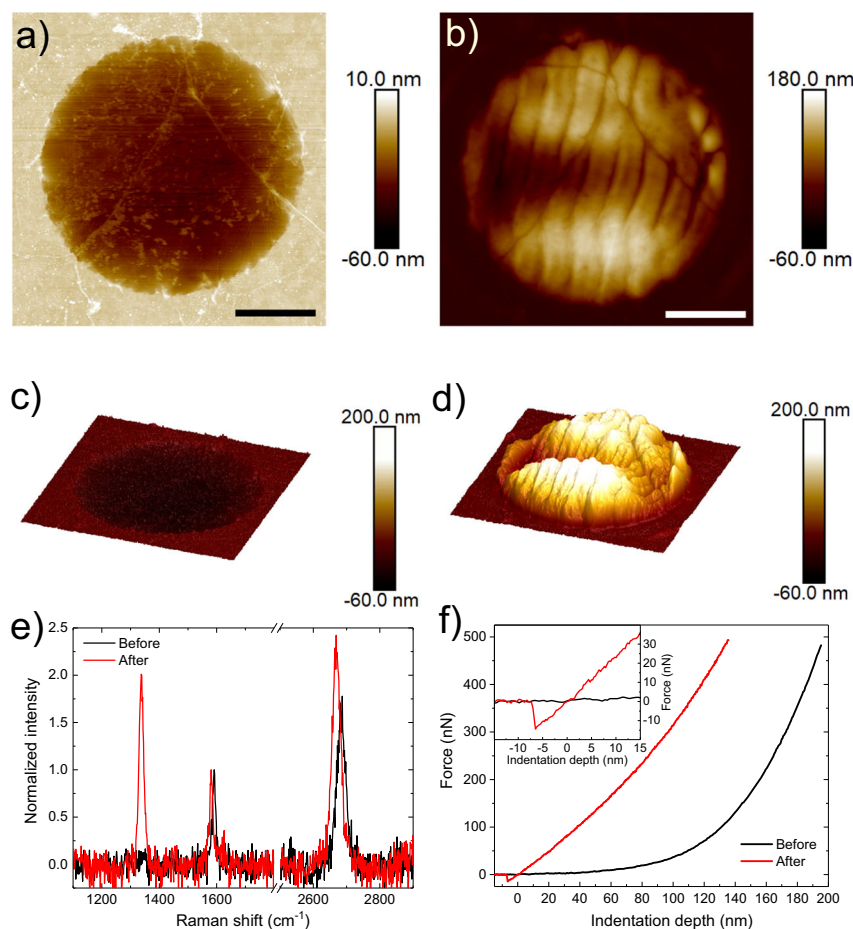


Fig. 1 Experimental results of a membrane irradiated with dose of $2.4 \cdot 10^{11} \text{ pJscm}^{-2}$ per point. AFM images showing the membrane **a** before and **b** after optical forging. Panels **c** and **d** show 3D-rendered images of **a** and **b** with the same colorscale. Raman spectra **e** and force curves **f** showing the graphene before (black) and after (red) forging. Note that in panels **c** and **d** the vertical dimension is sixfold enhanced compared to the lateral dimension. Scale bars are $1 \mu\text{m}$.

Since pristine suspended graphene should be undoped, it is safe to say that the hole doping is caused by polymethyl methacrylate (PMMA) residues from the transfer process¹¹. The AFM image in Fig. 1a shows some scattered residues of PMMA on the graphene surface. After the laser treatment both the G- and 2D-bands are downshifted, suggesting that both strain and doping are reduced. We attribute the decrease of doping to removal of these polymer residues by the forging. This cleaning effect can be seen from the AFM images in Fig. 1. The reduction of strain is a bit more surprising considering the large change in morphology, but we argue that this is an inherent property of the corrugated graphene. The trend of decreasing strain and doping is noticeable for all forged membranes (see Supplementary Methods).

Mechanical properties of optically forged graphene

Figure 1f shows examples of indentation curves before (black) and after (red) optical forging. The before curve shows typical behavior for a single-layer graphene membrane. It is clear already on the first inspection that the curve after the laser treatment is much more linear. This linear behavior indicates that either stress, bending stiffness or both increase during the treatment. The effect of forging is visible also in the zoomed inset, where the force falls below zero, signifying that the probe is snapping downwards into contact with the sample. The negative force is caused by long-range attractive interactions that cause the cantilever to deflect towards the surface. With pristine graphene (i.e., before optical forging) the attractive force is barely noticeable. This is because

single-layer graphene is very flexible in the direction perpendicular to its 2D lattice and as freestanding it is free to bend both upwards and downwards. Since it flexes easily, it cannot exert large bending to the probe's cantilever. However, the optically forged graphene is able to pull the cantilever down, giving another qualitative indication that the bending stiffness of the optically forged graphene is strongly increased. It is important to note here that, after the optical forging, the membrane morphology is fully stable. Even after the membrane is indented with a force of 500 nN, it reverts accurately back to the shape shown in Fig. 1b, d.

Mechanical properties of the graphene can be determined from a fit to indentation data. The relationship between the force and indentation depth for indentation at the center of a circular membrane is characterized by equation¹:

$$F = \left(\frac{16\pi D}{R^2} + \sigma_0^{2D} \right) \delta + \left(\frac{E^{2D} q^3}{R^2} \right) \delta^3, \quad (1)$$

where F is the indentation force, R is the membrane diameter, D is the bending stiffness, σ_0^{2D} is the film pretension, δ is the indentation depth, E^{2D} is the two-dimensional elastic modulus, and $q = 1/(1.05 - 0.15\nu - 0.16\nu^2)$ is a dimensionless constant, where ν is the Poisson's ratio. It is often difficult to determine the zero point of indentation, the point where the tip is touching the sample but not exerting any force to it. In order to make the fitting procedure independent of manual bias, we used the full third-order polynomial to fit the experimental data (see "Methods").

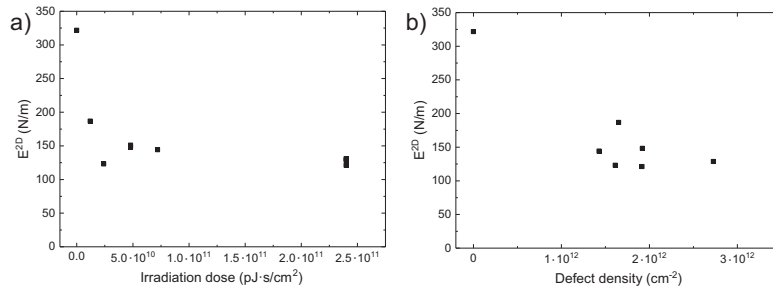


Fig. 2 The effect of optical forging on the 2D elastic modulus of graphene. **a** E^{2D} vs. pulsed laser irradiation dose per point. **b** E^{2D} vs. defect density.

Figure 2a shows the effect of optical forging dose on the two-dimensional elastic modulus of graphene. Before the optical forging, the average elastic modulus value for our membranes is 322 Nm^{-1} ($\sim 1 \text{ TPa}$), which is in good agreement with earlier works^{1,12}. When the graphene is optically forged, already the lowest doses decrease the elastic modulus below 200 Nm^{-1} . However, the highest doses do not seem to decrease it below 125 Nm^{-1} , which is likely because the defect density does not increase considerably when the dose is increased. The defect density was calculated from D- and G-bands of the membrane's Raman spectra (see Supplementary Methods). Figure 2b presents the elastic modulus as a function of defect density, showing how after the optical forging the defect density ranges between 1.4 and $2.7 \cdot 10^{12} \text{ cm}^{-2}$ and in this range does not really affect the elastic modulus after the initial decrease. The decrease in elastic modulus matches well with earlier simulation results¹³. In previous experimental studies the elastic modulus has been found to either increase¹⁴ or decrease¹⁵ with increasing defect density. An important factor in determining what happens is the type of defects. Monovacancies increase the elastic modulus of the membranes, while other defect types, like Stone-Wales type defects, cause lowering of the elastic modulus^{14,16}.

Determining the bending stiffness quantitatively from the indentation data is not straightforward. The bending stiffness for flat pristine single-layer graphene is very small, less than 10 eV^{17-20} . Therefore, the bending stiffness is normally negligible compared to pretension and fitting of the force curves are done without the first term in Eq. (1). This is also a good assumption in our case before forging. After forging the situation is not as simple, since a more pronounced linear trend in the curve could indicate higher pretension, higher bending stiffness, or both. However, as mentioned above, Raman data indicates that strain after the optical forging is lower, not higher. Additionally, high-bending stiffness values for graphene with corrugations has been reported before², and therefore the bending stiffness cannot be assumed to be negligible after forging. Since the bending stiffness and pretension are assumed to be of the same magnitude, they cannot be separated using only the indentation data. Therefore, we calculated the tension from Raman data using the analysis described by Lee et al.¹⁰. First, we calculated the tension from nonirradiated graphene both from the indentation fit parameters and Raman data to check the reliability of Raman spectroscopy for this purpose. The results are presented in Table 1, and they show a surprisingly good match between the methods, giving us assurance that the tension can be calculated reliably from Raman data. Bending stiffness of optically forged graphene membrane can then be calculated by subtracting the pretension from the linear term of the indentation fit.

Figure 3 shows AFM images and force-indentation depth curves for three different membranes. All of the AFM images are taken after optical forging. Insets in Fig. 3b, d, and f show the snap-to-contact region and have the same scale to ease comparison. In

Membrane	Raman (Nm^{-1})	Indentation (Nm^{-1})
1	0.128	0.104
2	0.099	0.100
3	0.139	0.166
4	0.114	0.130
5	0.155	0.179
6	0.158	0.179

Fig. 3a the graphene membrane does not have clearly developed corrugation and the force curves before and after the laser treatment are very similar in shape. The membrane in Fig. 3c is slightly corrugated from the sides of the membrane and the force curve in Fig. 3d shows slight change. In Fig. 3e the membrane has clearly more corrugated structure compared to the previous two. Consequently, the force curve after the laser treatment has a clear snap-in and the curve is initially much more linear. The extreme situation is presented in Fig. 1, where the membrane is very corrugated and the force curve is almost fully linear. Note that also the diameter of the openings in Fig. 3a, c, and e increase in this order. Bending stiffness calculated as described above yield 3 keV (a,b), 19 keV (c,d), 93 keV (e,f) and 790 keV (Fig. 1). Note that, based on the noise level of our AFM system and the indentation data from the nonirradiated membranes, the minimum bending stiffness value that we can reliably measure is $\sim 20 \text{ keV}$. Therefore, we can only say that the stiffnesses of the membranes in Fig. 3a–d are somewhere below 20 keV . However, the values for membranes in Figs. 3e and Fig. 1 are well above the threshold, and extremely high for graphene: the 0.8 MeV stiffness is the highest ever reported for graphene by two orders of magnitude². While it makes sense to see a hugely increased stiffness when the changes in the membrane morphology and force curve are as large as in Fig. 1, this matter requires investigation also from a theoretical standpoint.

Dynamical simulations of forged graphene membranes

To better understand the role of corrugations, we modeled indentation experiments by computer simulations. Simulations used a classical thin-sheet elasticity model, which captures graphene's behavior well both at atomic and mesoscopic length scales^{21–27}. The strain parameter $k_s = 336 \text{ Nm}^{-1}$ was set equal to a typical value for a flat, pristine graphene membrane^{3,12,22}. However, because of the unknown microstructure of optically forged graphene, the bending parameter k_b was treated as an adjustable parameter². Note that k_s and k_b are parameters *intrinsic* to the model and represent material properties below the used 20 nm discretization length scale. Generally they differ from the

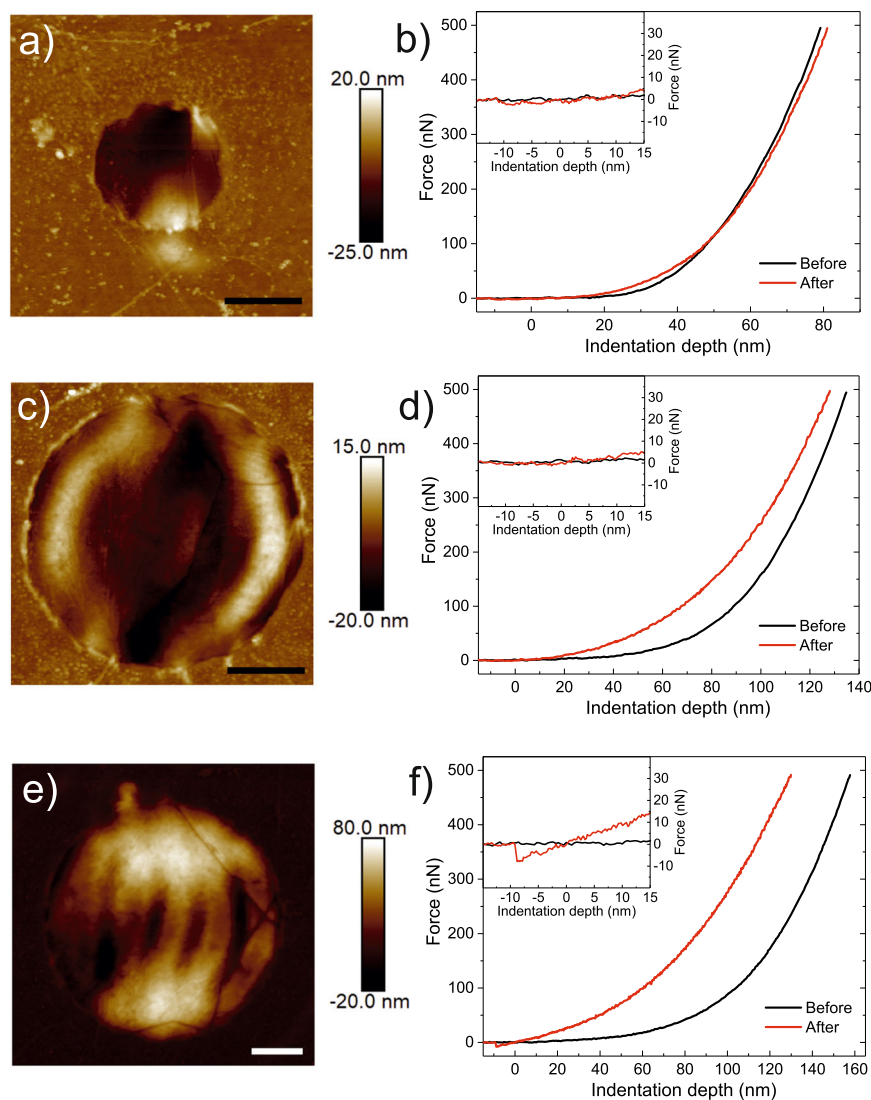


Fig. 3 AFM images and force-indentation curves for three different membranes. Irradiation dose for membranes in **a** and **c** was $4.8 \cdot 10^{10}$ pJscm^{-2} per point and for **e** $7.2 \cdot 10^{10}$ pJscm^{-2} . Panels on the right show the force-indentation curves of the membranes shown in the left, respectively. Curves are measured both before (black) and after (red) optical forging. Insets in the panels on the right show the snap-to-contact region. All the scale bars are 500 nm.

2D elastic modulus E^{2D} and bending stiffness D , which are quantities derived from the force-indentation curves through Eq. (1) and depend on membrane morphology. In short, indentation simulations proceeded by first defining the initial state for the membrane and then applying a gradually increasing and then decreasing force in the middle, while following the membrane's response by a dynamical simulation (for details, see "Methods").

We began by simulating the indentation of graphene before forging, represented here by an initially flat membrane with $k_s = 1$ keV (Fig. 4a). In this special case with $E^{2D} = k_s$, $D = k_b$, the force-indentation curve follows Eq. (1) closely, and zero pre-strain (Fig. 4e), as expected and in agreement with experiment (Fig. 1f). Following, we attempted to simulate the optically forged membrane in Fig. 1 by using the previous convention of forging-induced homogeneous and isotropic biaxial expansion^{3,4}, here derived from the AFM topography to be equal to $\varepsilon_0 = 2.3\%$. However, with homogeneous expansion, the experimental morphology turned out to be completely unstable and the membrane relaxed into an unrecognizable, featureless hump regardless of the value of k_b (Fig. 4b). Similar instabilities occurred for other experimental morphologies (Fig. 3). These instabilities imply that

the previous convention of homogeneous expansion is inappropriate and that the expansion fields are non-homogeneous and membrane morphologies are *frozen*: morphology defines the adaptation to a new state of zero elastic energy.

To build on this idea, we simulated the indentation of a membrane with $k_b = 1$ keV adapted to the morphology in Fig. 4c². The indentation process was reversible and the topography recovered accurately after maximum indentation depth of 360 nm, in agreement with the experiment (Fig. 4d; see also Supplementary Video). Owing to the hidden area related to corrugations, the force-indentation curve becomes overall more shallow than for the flat membrane (Fig. 4e)²⁸. However, the scale of the figure does not reveal the most significant difference at small indentation depths: by fitting Eq. (1) to the force-indentation curve, the bending stiffness comes with the value of $D = 61$ keV. Although smaller than D in the experiment, it is still nearly two orders of magnitude larger than the bending parameter k_b . The reason for this stiffening is corrugation. Theory has shown that, in the presence of corrugations, bending stiffness behaves as

$$D = \sqrt{k_s k_b (h^2)}, \quad (2)$$

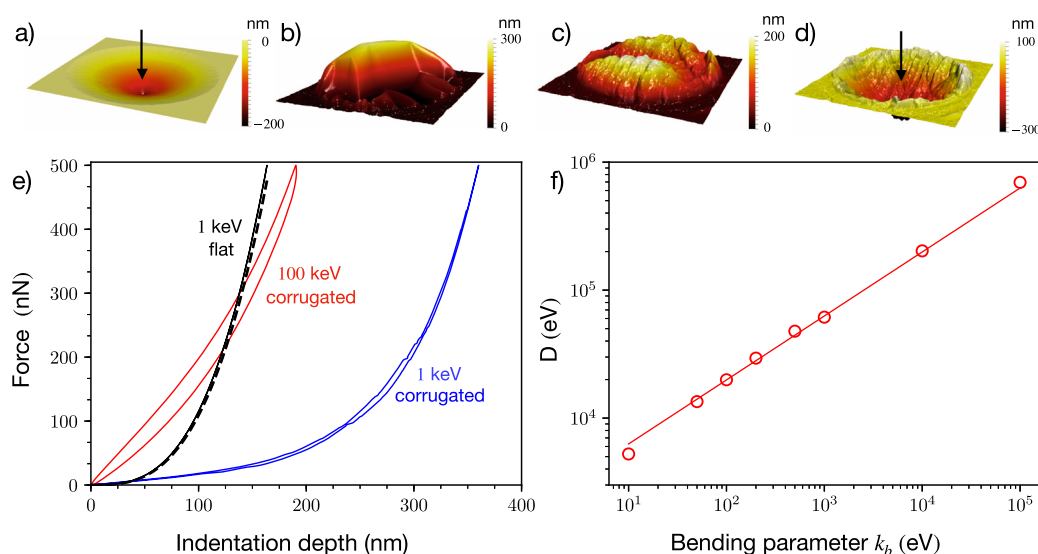


Fig. 4 Simulating indentation by thin-sheet elasticity theory. **a** Flat membrane over a 3.4- μm -diameter hole with 500 nN force applied in the middle. **b** Optimized geometry of a membrane with homogeneous and isotropic expansion of $\varepsilon_0 = 2.3\%$ inferred from the morphology in panel **c** and using the same morphology as the initial guess. **c** Morphology of Fig. 1b to which membrane was adapted before indentation simulation (reproduced here for easy comparison); the same morphology was recovered after indentation. **d** Corrugated membrane at 500 nN force applied in the middle. **e** Force-indentation curves for flat membrane with $k_b = 1$ eV (black curve), corrugated membrane with $k_b = 1$ keV (blue curve), and corrugated membrane with $k_b = 100$ keV (red curve). Dashed curve is Eq. (1) with $D = 1$ keV and $E^{2D} = 336 \text{ Nm}^{-1}$. Curves show small hysteresis for corrugated membranes. **f** Bending moduli D derived from the curves for different bending parameters k_b (circles), with a fit to Eq. (2) (solid line). All images show $3.7 \times 3.7 \mu\text{m}$ area with $k_b = 1$ keV, hole diameter 3.4 μm , and vertical dimension fourfold enhanced.

where $\langle h^2 \rangle$ is the mean square deviation of the height corrugations^{29,30}. To confirm this behavior, we adapted the membrane to the same morphology and calculated $D(k_b)$ for various k_b (Fig. 4f) and made a fit to Eq. (2) using $\Delta h = \sqrt{\langle h^2 \rangle}$ as a fit parameter. The fit gave $\Delta h = 42$ nm, in good agreement with the simulated values of $D(k_b)$ and in excellent accordance with the value $\Delta h_{\text{AFM}} = 43$ nm, determined independently and directly from the AFM topography over the hole area. Therefore, based on Eq. (2) and direct simulations (cf. Figs. 1f and 4e), the experimental stiffness $D = 0.8$ MeV implies bending parameter of $k_b \sim 100$ keV for this particular sample of optically forged graphene. These results imply that, in addition to corrugation-induced stiffening at mesoscale, optical forging stiffens graphene substantially also at the nanoscale.

DISCUSSION

To conclude, our results show that optical forging can be used to substantially enhance the bending stiffness of monolayer graphene by forming fully stable corrugated structures. Raman spectra verified that optical forging creates defects in the graphene lattice, but the graphene remains single-layered with long-range order. Nanoindentation study revealed that the bending stiffness of the corrugated graphene membranes can increase up to 0.8 MeV, record high for graphene by two orders of magnitude². Although astonishing in magnitude, the reported bending modulus is still a realistic one. Bles and co-workers already reported 1–10 keV bending moduli in kirigami samples made of CVD-grown graphene². In other words, the intrinsic bending modulus of “pristine” CVD graphene can be 3–4 orders of magnitude larger than the theoretical bending modulus of ideally flat graphene. Here optical forging corrugates graphene visibly, which accordingly enhances bending modulus substantially more. Our simulations show that the corrugations observed by AFM enhanced the measured bending modulus by an additional 1–2 orders of magnitude compared to the intrinsic bending modulus (Fig. 4f), in accordance with recent reports³¹. In simple terms, this stiffening becomes possible because corrugations couple bending

to graphene’s large in-plane stiffness through stretching and compression. However, further investigations are required to clarify and fully quantify the scale-dependence of the bending modulus, starting from the defected atomic structure.

These findings may open new avenues to build a plethora of new nanomechanical structures and metamaterials where besides being light and strong, graphene is also made extremely stiff. For example, it could serve as an ultralight scaffold or reinforcement in microelectromechanical structures. It also has potential in creating active components in sensing, where the stiffness can be tuned locally by optical forging. One example is mechanical resonators, where graphene already is considered a promising material due to its strength and lightweight. It has been shown that circular graphene membranes with similar radius to our membrane in Fig. 1 have typical resonance frequencies in the range of a few tens of MHz^{32–34}. Since $f \propto \sqrt{D}$, stiffening of the graphene membrane can then be used to modify the fundamental resonance frequency of the resonator³⁵. The observed bending stiffness increase from a few eV up to 0.8 MeV would bring the fundamental mechanical resonance frequency into the GHz range. The only previous demonstration of reaching the GHz range is by strongly straining the graphene membrane, which is a difficult method to control³⁶. Optical forging on the other hand provides controlled defect engineering that modifies the bending stiffness, allowing tuning of the membrane resonance frequency. If assuming the quality factor (Q) is in the range of 100–1000 as for pristine graphene (it may even be higher depending on what dissipation channels are active), the membrane may allow coherent quantum operations at room temperature³⁷. Finally, the same stiffness modification demonstrated here for graphene may apply for other 2D materials as well.

METHODS

Fabrication of suspended graphene sample

Graphene used in the indentation experiments was synthesized using chemical vapor deposition. First, a catalyst surface was fabricated by

evaporating 600 nm copper film onto a cleaned single crystal Al_2O_3 (0001) surface. Then the sample was placed into a furnace (MTI, GSL-1100X) for annealing and graphene synthesis. Annealing was performed at 1050 °C under gas flows of 470 sccm argon and 30 sccm hydrogen for 30 min. The annealing step cleans impurities from the copper surface and also crystallizes the copper forming (111) crystal plane via secondary grain growth^{38,39}. The synthesis of graphene was initiated directly after the annealing step by adding 3 sccm of 1 % CH_4 in argon gas mixture into the stream for 20 min, after which the sample was pulled out of the furnace and allowed to cool down.

After the synthesis the sample was spin-coated with PMMA support layer (PMMA A4, 3000 rpm) and placed to 1 M ammonium persulfate bath to etch the copper. After the copper etching the graphene/PMMA stack was rinsed with deionized water and placed onto a 300 nm thick silicon nitride membrane window with etched circular openings of different sizes. The sample was allowed to dry overnight after which it was baked on a hot plate at 100 °C for 5 min to remove as much residual water between the graphene and the substrate as possible. The PMMA was then removed using acetone and the sample was dried with a critical point dryer. This left graphene suspended over the openings. Then, in order to remove residual PMMA, the sample was annealed at 300 °C under gas flows of 400 sccm argon and 30 sccm hydrogen for two hours. After the annealing process, only scattered PMMA residues of 1–2 nm in height remain on the graphene surface, as visible in Fig. 1a.

Optical forging

Direct laser writing (optical forging) of the patterns was performed with 515 nm femtosecond laser (Pharos-10, Light Conversion Ltd., 600 kHz repetition rate, 250 fs pulse duration) focused with an objective lens (N.A. = 0.8) to a single Gaussian spot (FWHM ~ 500 nm)³. The spot size has been estimated using small sized openings in the Si_3N_4 window. With 500 nm opening size a small reflection ring is visible, while with 800 nm opening no reflection is observed. The laser writing was performed under a nitrogen purge to prevent photo-oxidation of graphene during the writing process. Pulse energy was 60 pJ in all exposures. For each membrane the writing pattern was a square covering the opening, for example with a 3.3 μm -diameter opening the patterned square size was $4 \times 4 \mu\text{m}^2$. The patterning was done by step-by-step irradiation with 0.1 μm separation between consecutive laser spots and writing speed varying from 0.5 to 10 s per spot for different membranes.

Raman spectroscopy

The membranes were characterized by Raman spectroscopy using a home-built Raman setup in backscattering geometry. Excitations were done with 532 nm CW laser (Alphas, Monolas-532-100-SM). The beam was focused to the sample and subsequently collected with a 100x microscope objective (Nikon, L Plan SLWD 100x/0.70). The scattered light was dispersed in a 0.5 m imaging spectrograph (Acton, SpectraPro 2500i) using a 600 g mm^{-1} grating (resolution: ~7–8 cm^{-1}). The signal was detected with an EMCCD camera (Andor Newton, EM DU971N-BV) using 100 μm slit width. A beam splitter was placed between the objective and the spectrometer in order to observe the exact measurement point visually. The Rayleigh scattering was attenuated with an edge filter (Semrock). The incident laser power was 0.1 mW.

Atomic force microscopy and nanoindentation

The sample was imaged using an atomic force microscope (Bruker, Dimension Icon) with PeakForce tapping mode. During imaging we used ScanAsyst Air probes with nominal spring constant of 0.4 Nm^{-1} .

Indentation was done with the same AFM setup as the imaging using diamond-like carbon coated Tap300 probes (Budget Sensors). The spring constants of the probes were calibrated by indenting the silicon nitride substrate. The spring constants ranged between 38 and 58 Nm^{-1} . Radii of the probes were determined from a scanned image of high roughness titanium sample (Bruker)^{40,41}. Based on the AFM imaging, graphene membranes that did not have holes or too much impurities were used for indentation experiments. The same graphene membranes were indented both before and after the direct laser writing in order to have directly comparable results. A total of eight different graphene membranes were studied. For each membrane five force vs. indentation depth curves with 500 nN maximum force were collected. For each membrane the first indentation curve was excluded, because in the first indentations the

elastic modulus value calculated from the fitting parameters were systematically lower than with the rest of the indentations. This was caused by membrane slipping when load was applied to the membrane and has been reported previously⁴².

A common problem with indentation measurements of thin materials is the determination of the zero point of indentation. To overcome this issue, we used the full third-order polynomial form of Eq. (1), which has been used also in previous studies^{14,42}. By writing $F = f - f_0$ and $\delta = Z - \delta_0$, where f is the measured force, Z the piezo movement in z direction, f_0 and δ_0 are free parameters and $k_1 = \frac{16\pi D}{R^2} + \sigma_0^{2D}\pi$ and $k_2 = E^{2D}q^3/R^2$ are linear and cubic coefficients, Eq. (1) becomes

$$f - f_0 = k_1(Z - \delta_0) + k_2(Z - \delta_0)^3. \quad (3)$$

For fitting this can be written as

$$f = (f_0 - k_1\delta_0 - k_2\delta_0^3) + (k_1 + 3k_2\delta_0^2)Z - (3k_2\delta_0)Z^2 + k_2Z^3. \quad (4)$$

By using this fitting function, human input is not required for picking the zero point of indentation. This point can be determined from the fitting parameters f_0 and δ_0 .

Thin-sheet elasticity simulations

The indentation experiments were simulated by thin-sheet elasticity theory, which is known to model graphene well over several length scales^{3,21,22,24}. The total energy of the sheet is obtained by integrating in-plane strain, out-of-plane bending, and external energy densities

$$E = \int (f_s + f_b + f_{\text{ext}}) dA. \quad (5)$$

The in-plane strain energy density is

$$f_s = \frac{k_s}{1 - \nu^2} \left[\frac{1}{2} (\epsilon_{xx} + \epsilon_{yy})^2 - (1 - \nu) (\epsilon_{xx}\epsilon_{yy} - \epsilon_{xy}^2) \right], \quad (6)$$

where $\epsilon_{\alpha\beta}(\mathbf{r})$ is the strain tensor, $\nu = 0.165$ is the Poisson ratio, and $k_s = 336 \text{ Nm}^{-1}$ is the strain parameter^{3,12}. The bending energy density is

$$f_b = \frac{k_b}{2} \left[(C_{xx} + C_{yy})^2 - 2(1 - \nu) (C_{xx}C_{yy} - C_{xy}^2) \right], \quad (7)$$

with bending modulus k_b and curvature tensor $C_{\alpha\beta}(\mathbf{r})$ ⁴³. The external energy density f_{ext} is a delta-function-type potential that inflicts a predetermined downward force $\mathbf{F} = -F\mathbf{k}$ dead center of the membrane.

The expansion field $\epsilon_{\alpha\beta}^e(\mathbf{r})$ due to optical forging is introduced through a modified strain tensor $\epsilon_{\alpha\beta}(\mathbf{r}) = \epsilon_{\alpha\beta}^p(\mathbf{r}) - \epsilon_{\alpha\beta}^e(\mathbf{r})$, where $\epsilon_{\alpha\beta}^p(\mathbf{r})$ is the strain tensor of the unexpanded, pristine membrane^{3,4}. Homogeneous and isotropic expansion by ϵ_0 is given by $\epsilon_{\alpha\beta}^e(\mathbf{r}) = \epsilon_0\delta_{\alpha\beta}$. By treating the curvature tensor analogously, the membrane is adapted to a given morphology by defining non-homogeneous expansion and curvature fields $\epsilon_{\alpha\beta}^e(\mathbf{r})$ and $C_{\alpha\beta}^e(\mathbf{r})$ such that the elastic energy density at that morphology is identically zero.

Using this theory, a $3.7 \times 3.7 \mu\text{m}$ square membrane was discretized to a square lattice with $dx = 20 \text{ nm}$ spacing. The square had a 3.4- μm -diameter hole in the middle, outside of which the lattice points were fixed and inside of which they were propagated using Langevin thermostat at 300 K temperature. Thermostat's damping time was $\tau = d/v_{\perp}$, where d is hole diameter and $v_{\perp} = 60 \times \sqrt{k_b/\text{eV}} \text{ ms}^{-1}$ is the speed of transverse waves at relevant wavelengths. This choice was made to allow transverse waves enough time to propagate across the membrane before dissipation. The time step was $dt = dx/4v_{\parallel}$ (0.25 ps at maximum), where $v_{\parallel} = 22 \text{ kms}^{-1}$ is the speed of longitudinal waves.

The simulations proceeded by increasing the indentation force gradually from zero to $F_{\text{max}} = 500 \text{ nN}$ and reducing it back to zero, within 1000 force steps. Elastic waves generated by steps in force were allowed to dissipate for the duration of one damping time τ , resulting in a total simulation time of $t_{\text{tot}} = 1000 \times \tau$.

DATA AVAILABILITY

All data used in this study are available from the corresponding author upon reasonable request.

Received: 2 November 2020; Accepted: 26 March 2021;
Published online: 12 May 2021

REFERENCES

- Lee, C., Wei, X., Kysar, J. W. & Hone, J. Measurement of the elastic properties and intrinsic strength of monolayer graphene. *Science* **321**, 385–388 (2008).
- Blees, M. K. et al. Graphene kirigami. *Nature* **524**, 204–207 (2015).
- Johansson, A. et al. Optical forging of graphene into three-dimensional shapes. *Nano Lett.* **17**, 6469–6474 (2017).
- Koskinen, P. et al. Optically forged diffraction-unlimited ripples in graphene. *J. Phys. Chem. Lett.* **9**, 6179–6184 (2018).
- Hiltunen, V.-M. et al. Making graphene luminescent by direct laser writing. *J. Phys. Chem. C* **124**, 8371–8377 (2020).
- Torres, J., Zhu, Y., Liu, P., Lim, S. C. & Yun, M. Adhesion energies of 2D graphene and MoS₂ to silicon and metal substrates. *Phys. Status Solidi A* **215**, 1700512 (2018).
- Ferrari, A. C. et al. Raman spectrum of graphene and graphene layers. *Phys. Rev. Lett.* **97**, 187401 (2006).
- Ferrari, A. C. Raman spectroscopy of graphene and graphite: disorder, electron–phonon coupling, doping and nonadiabatic effects. *Solid State Commun.* **143**, 47–57 (2007).
- Beams, R., Cañado, L. G. & Novotny, L. Raman characterization of defects and dopants in graphene. *J. Phys. Condens. Matter* **27**, 083002 (2015).
- Lee, J. E., Ahn, G., Shim, J., Lee, Y. S. & Ryu, S. Optical separation of mechanical strain from charge doping in graphene. *Nat. Commun.* **3**, 1024 (2012).
- Pirkle, A. et al. The effect of chemical residues on the physical and electrical properties of chemical vapor deposited graphene transferred to SiO₂. *Appl. Phys. Lett.* **99**, 122108 (2011).
- Lee, G.-H. et al. High-strength chemical vapor-deposited graphene and grain boundaries. *Science* **340**, 1073–1076 (2013).
- Jing, N. et al. Effect of defects on Young's modulus of graphene sheets: a molecular dynamics simulation. *RSC Adv.* **2**, 9124–9129 (2012).
- López-Polín, G. et al. Increasing the elastic modulus of graphene by controlled defect creation. *Nat. Phys.* **11**, 26–31 (2015).
- Zandiatashbar, A. et al. Effect of defects on the intrinsic strength and stiffness of graphene. *Nat. Commun.* **5**, 3186 (2014).
- Kvashnin, D. & Sorokin, P. Effect of ultrahigh stiffness of defective graphene from atomistic point of view. *J. Phys. Chem. Lett.* **6**, 2384–2387 (2015).
- Nicklow, R., Wakabayashi, N. & Smith, H. G. Lattice dynamics of pyrolytic graphite. *Phys. Rev. B* **5**, 4951–4962 (1972).
- Koskinen, P. & Kit, O. O. Approximate modeling of spherical membranes. *Phys. Rev. B* **82**, 235420 (2010).
- Lindahl, N. et al. Determination of the bending rigidity of graphene via electrostatic actuation of buckled membranes. *Nano Lett.* **12**, 3526–3531 (2012).
- Wei, Y., Wang, B., Wu, J., Yang, R. & Dunn, M. L. Bending rigidity and Gaussian bending stiffness of single-layered graphene. *Nano Lett.* **13**, 26–30 (2013).
- Landau, L. D. & Lifshitz, E. M. *Theory of Elasticity* (Pergamon, New York, 1986).
- Kudin, K., Scuseria, G. & Yakobson, B. C₂F, BN, and C nanoshell elasticity from ab initio computations. *Phys. Rev. B* **64**, 235406 (2001).
- Koskinen, P. Electronic and optical properties of carbon nanotubes under pure bending. *Phys. Rev. B* **82**, 193409 (2010).
- Kit, O. O., Tallinen, T., Mahadevan, L., Timonen, J. & Koskinen, P. Twisting graphene nanoribbons into carbon nanotubes. *Phys. Rev. B* **85**, 085428 (2012).
- Ramasubramaniam, A., Koskinen, P., Kit, O. O. & Shenoy, V. B. Edge-stress-induced spontaneous twisting of graphene nanoribbons. *J. Appl. Phys.* **111**, 054302 (2012).
- Korhonen, T. & Koskinen, P. Electromechanics of graphene spirals. *AIP Adv.* **4**, 460127125 (2014).
- Koskinen, P. Graphene cardboard: from ripples to tunable metamaterial. *Appl. Phys. Lett.* **104**, 101902 (2014).
- Nicholl, R. J., Lavrik, N. V., Vlasiouk, I., Srijanto, B. R. & Bolotin, K. I. Hidden area and mechanical nonlinearities in freestanding graphene. *Phys. Rev. Lett.* **118**, 4651–4656 (2017).
- Kosmrlj, A. & Nelson, D. R. Mechanical properties of warped membranes. *Phys. Rev. E* **88**, 012136 (2013).
- Eletto, H. & Melo, F. *Wrinkled Polymer Surfaces*. 229–252 (Springer, 2019).
- Kähärä, T. & Koskinen, P. Rippling of two-dimensional materials by line defects. *Phys. Rev. B* **102**, 075433 (2020).
- Bunch, J. S. et al. Electromechanical resonators from graphene sheets. *Science* **315**, 490–493 (2007).
- Chen, C. et al. Performance of monolayer graphene nanomechanical resonators with electrical readout. *Nat. Nanotechnol.* **4**, 861–867 (2009).
- De Alba, R. et al. Tunable phonon-cavity coupling in graphene membranes. *Nat. Nanotechnol.* **11**, 741–746 (2016).
- Lima-Rodriguez, A., Gonzalez-Herrera, A. & Garcia-Manrique, J. Study of the dynamic behaviour of circular membranes with low tension. *Appl. Sci.* **9**, 4716 (2019).
- Jung, M. et al. GHz nanomechanical resonator in an ultraclean suspended graphene p–n junction. *Nanoscale* **11**, 4355–4361 (2019).
- Norte, R. A., Moura, J. P. & Gröblacher, S. Mechanical resonators for quantum optomechanics experiments at room temperature. *Phys. Rev. Lett.* **116**, 147202 (2016).
- Reddy, K. M., Gledhill, A. D., Chen, C.-H., Drexler, J. M. & Padture, N. P. High quality, transferrable graphene grown on single crystal Cu(111) thin films on basal-plane sapphire. *Appl. Phys. Lett.* **98**, 113117 (2011).
- Hu, B. et al. Epitaxial growth of large-area single-layer graphene over Cu(111)/sapphire by atmospheric pressure CVD. *Carbon* **50**, 57–65 (2012).
- Villarrubia, J. S. Algorithms for scanned probe microscope image simulation, surface reconstruction, and tip estimation. *J. Res. Natl Inst. Stand. Technol.* **102**, 102–425 (1997).
- Flater, E. E., Zacharakis-Jutz, G. E., Dumba, B. G., White, I. A. & Clifford, C. A. Towards easy and reliable AFM tip shape determination using blind tip reconstruction. *Ultramicroscopy* **146**, 130–143 (2014).
- Lin, Q.-Y. et al. Stretch-induced stiffness enhancement of graphene grown by chemical vapor deposition. *ACS Nano* **7**, 1171–1177 (2013).
- do Carmo, M. P. *Differential Geometry of Curves and Surfaces*, (Prentice Hall, 1976)

ACKNOWLEDGEMENTS

V.-M.H. acknowledges funding from the Finnish Cultural Foundation. P.K. and M.P. acknowledge funding from the Academy of Finland (grants 297115 and 311330).

AUTHOR CONTRIBUTIONS

V.-M.H., M.P. and A.J. designed the study. V.-M.H. prepared the sample and carried out measurements and analysis. P.K. performed computer simulations. K.M. performed optical forging. V.-M.H. and P.K. wrote the manuscript. M.P. and A.J. supervised the study. All authors reviewed and commented on the manuscript.

COMPETING INTERESTS

The authors declare no competing interests.

ADDITIONAL INFORMATION

Supplementary information The online version contains supplementary material available at <https://doi.org/10.1038/s41699-021-00232-1>.

Correspondence and requests for materials should be addressed to A.J.

Reprints and permission information is available at <http://www.nature.com/reprints>

Publisher's note Springer Nature remains neutral with regard to jurisdictional claims in published maps and institutional affiliations.



Open Access This article is licensed under a Creative Commons Attribution 4.0 International License, which permits use, sharing, adaptation, distribution and reproduction in any medium or format, as long as you give appropriate credit to the original author(s) and the source, provide a link to the Creative Commons license, and indicate if changes were made. The images or other third party material in this article are included in the article's Creative Commons license, unless indicated otherwise in a credit line to the material. If material is not included in the article's Creative Commons license and your intended use is not permitted by statutory regulation or exceeds the permitted use, you will need to obtain permission directly from the copyright holder. To view a copy of this license, visit <http://creativecommons.org/licenses/by/4.0/>.

© The Author(s) 2021